Progress In Electromagnetics Research B, Vol. 101, 63–84, 2023

Performance Improvement of Antenna Using Metasurface: An Overview

Naresh C. Naik, Nibash K. Sahu*, Bijay K. Ekka, and Tapas K. Patra

Abstract—This paper presents an in-depth review of the performance improvement of antennas using metasurface. Metasurface is a periodic arrangement of perfect electric conductors (PECs) on a metal-backed dielectric substrate that do not exist in nature and are able to manipulate the behavior of electromagnetic (EM) waves incident on it. The manipulations of EM waves improve the performances in terms of impedance bandwidth, gain, size, specific absorption rate (SAR), radar-cross-section (RCS), and polarization conversions. Consequently, numerous recent works on metasurface-inspired antenna design and their theoretical perspectives on performance enhancements are discussed. By adopting the discussed theories, novel metasurfaces are developed and proposed that analyze impedance-bandwidth enhancement, gain enhancement, and SAR reduction. For designing the metasurfaces, initially a conventional rectangular unit cell (CRUC) is theoretically developed using transmission line model at 2.45 GHz. Following that, the CRUC-based metasurface is incorporated with a monopole antenna, which enhanced the impedance-bandwidth from 140 MHz to 320 MHz and the gain from 2.5 dB to 7.4 dB. On the body, the presence of the metasurface retains all the performances as free space, with a reduced 1 g SAR of 0.034 and 10 g SAR of 0.024 W/kg.

1. INTRODUCTION

In the modern era of technology, academics, researchers, and engineers are increasingly focusing on the development of unique metasurfaces due to their extensive use in wireless communication at microwave frequencies [1–3]. Metasurface is a form of metamaterial [4–13] where metallic unit cells are arranged on the surface of metal-backed two-dimensional dielectric substrates. These arrangements, along with the specific shape, geometry, and size of the structures, can influence EM manipulation and possess certain beneficial characteristics that do not occur in nature. The beneficial characteristics include the blocking, absorbing, and bending of EM waves for a certain range of frequencies, which is not possible using conventional materials. These metasurface functionalities classify metasurface as an artificial magnetic conductor (AMC) [14–16], high impedance surface (HIS) [17, 18], and electromagnetic band gap (EBG) [19, 20]. AMC and HIS possess the same type of characteristics, which are perfect magnetic conductor (PMC) behaviors, whereas the EBG possesses not only PMC-like behavior but also suppresses the surface wave flowing on it over a certain range of frequencies known as band gap. The above metasurface may use metallic vias between the ground plane and unit-cell through the dielectric substrate to increase inductance. This type of structure is known as a mushroom-like structure. The absence of metallic vias is known as via-free metasurface or uni-planar metasurface [3].

The manipulation of propagation of EM wave by the metasurface enhances the antenna performances. To summarize the application of metasurfaces and their development for performance improvement, researchers have proposed review articles [21, 22]. These articles have addressed the

---

Received 5 May 2023, Accepted 22 June 2023, Scheduled 9 July 2023

* Corresponding author: Nibash Kumar Sahu (nibash11@gmail.com).
The authors are with the Department of Electronics & Instrumentation Engineering, Odisha University of Technology and Research, Bhubaneswar, Odisha, India.

enhancement of bandwidth, gain, size, additional band generation, transmission between two antennas, SAR reductions, as well as the design and simulation of a metasurface. Apart from the review on the aforementioned performance improvement, there is also a need for a review on advances in polarization conversions and RCS reductions. The fact is that the polarization conversion mechanism can generate circular polarization (CP) characteristics that reduce the polarization mismatch loss associated with linear polarization (LP), and with a reduced RCS, vehicles are able to better avoid radar detection by land-based systems, guided missiles, and other vehicles.

This article emphasizes the review of the performance improvement that includes impedance bandwidth enhancement, gain enhancement, size reduction, SAR reduction, RCS reduction, and polarization conversion using metasurface, along with the theoretical mechanisms and a comparison table of previous works for each case. In addition, to analyze the performances, novel metasurfaces are developed and proposed. To design metasurfaces, initially a CRUC is theoretically designed using transmission line model to resonate at 2.45 GHz. Following that, CRUC-based metasurfaces are incorporated with monopole antennas to analyze bandwidth enhancement, gain enhancement, and SAR reduction using simulation software. Moreover, the CRUC is modified using square-type and L-type slots to analyze miniaturizations and polarizations, respectively. The paper is structured as follows. The theoretical mechanism of performance enhancement using metasurfaces is discussed in Section 2. In Section 3, the most recent developments in antenna performance using metasurfaces are presented. Section 4 presents the design and discussion of proposed metasurfaces, followed by a conclusion in Section 5.

2. THEORETICAL MECHANISM OF PERFORMANCE IMPROVEMENT

In the modern era of technology, academics, researchers, and engineers are increasingly focusing on the development of unique metasurfaces. These elements possess unique characteristics that can influence the propagation of EM waves and enhance the antenna's performance. This section discusses the theoretical mechanisms of performances using metasurfaces.

The unique reflection phase characteristic between 0° and 180° possessed by metasurfaces, as depicted in Figure 1(a) [23], which is not achievable by perfect electric conductors (PECs) that possess 180° reflected phase and PMC surfaces that possess 0° reflected phase, is mainly responsible for gain enhancement, bandwidth enhancement, and SAR reduction [24–27]. The metasurface facilitates high surface impedance in the frequency range where phase lies between -90° and $+90^\circ$, and the frequency range where phase lying between $90^\circ \pm 45^\circ$ can only be used for performances improvement [28, 29]. Therefore, the estimation of reflection phase characteristics is an important parameter to know the frequency range for in phase reflection from the metasurfaces upon the incident of a plane wave on them. For an in-depth understanding of reflection phase mechanism, the mushroom-like metasurface [28] proposed by Sievenpiper et al. is depicted in Figure 1(a). Figure 1(b) depicts its parameters; Figure 1(c) depicts the LC model; and Figure 1(d) depicts generalized equivalent circuit models. For high surface impedance, the circuit is treated as a parallel resonant circuit. From the equivalent circuit, the reflection coefficient (Γ), surface impedance (Z_s), resonant frequency (f_r), and bandwidth (BW) are given as follows:

$$\Gamma = \frac{Z_s - \eta_0}{Z_s + \eta_0} \tag{1}$$

$$Z_s = \frac{jwL}{1 - w^2 LC} \tag{2}$$

$$f_r = \frac{1}{2\pi\sqrt{LC}} \tag{3}$$

$$BW = \frac{1}{\eta_0}\sqrt{\frac{L}{C}} \tag{4}$$

The grid capacitance (C) generated by the gap between the unit cells and the inductance (L)

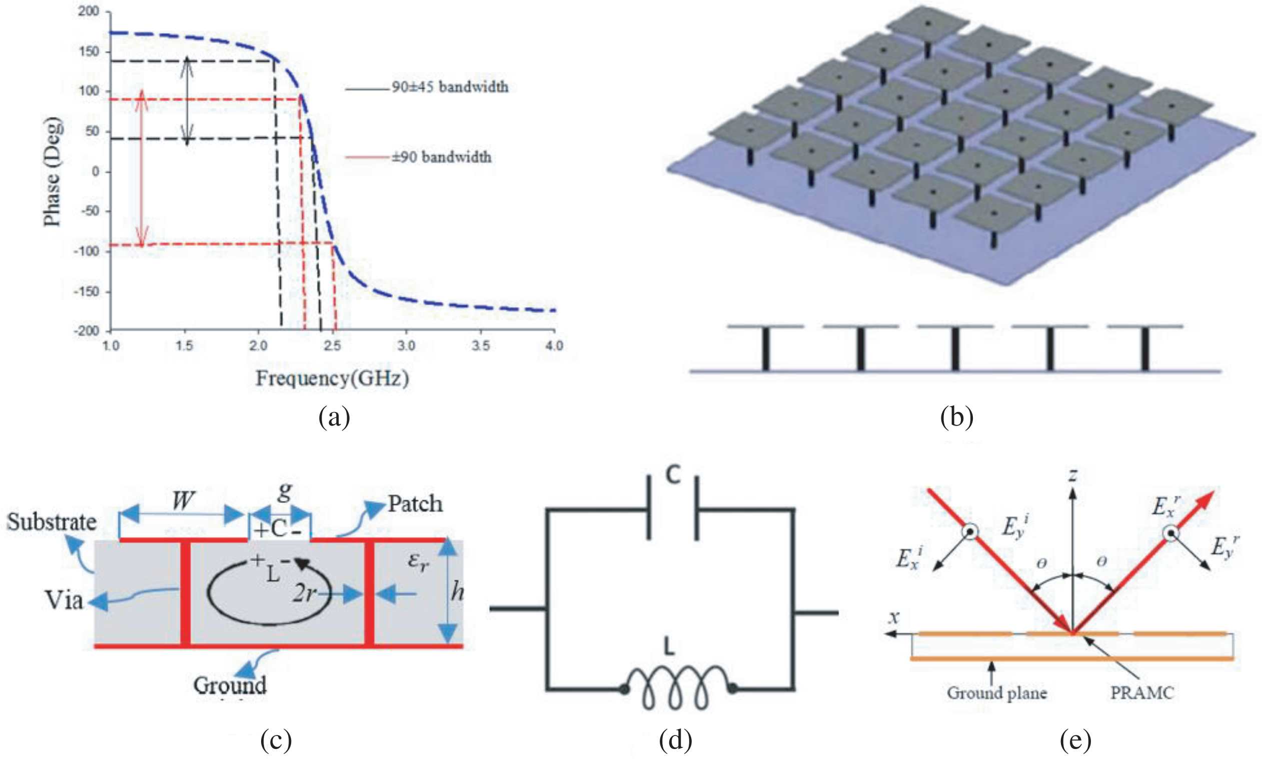

(a) (b)

(c) (d) (e)

Figure 1. (a) Reflection-phase characteristics [23], (b) structures of mushroom-like metasurfaces, (c) LC model, (d) generalized-circuit-model [28], and (e) polarization conversion mechanism by a Polarization Conversion Metasurface (PCMS) [25].

generated by the flow of current in the metallic via are given as follows [29]:

$$C = \frac{W\varepsilon_0(1+\varepsilon_r)}{\pi}\cosh^{-1}\left(\frac{W+g}{g}\right) \tag{5}$$

$$L = 2\times 10^{-7}h\left[\ln\left(\frac{2h}{r}\right)+0.5\left(\frac{2r}{h}\right)-0.75\right] \tag{6}$$

where ε_0 = free space permittivity, ε_r = dielectric constant of substrate, h = height of the substrate, r = radius of the pin, W = width of the unit-cell, and g = gap between the unit cells.

In the case of mushroom-type metasurfaces, the presence of metallic via causes discomfort in wearable applications and complicates fabrication. Nevertheless, the researchers of [30, 31] stated that, in the absence of metallic via, the metal-backed substrate can act as a short transmission line, and with a thickness of less than a quarter wave length, it generates an inductance L_d, which is known as dielectric slab inductance. The dielectric slab inductance can be represented as

$$L_d = \mu_0 h \tag{7}$$

where μ_0 = free space permeability.

Equation (3) indicates that the unit-cell is inductive below the resonance, that is, at a lower frequency, and hence a transverse magnetic (TM) wave is propagating on the surface. Upon reaching the resonant frequency, that is, at a higher frequency band, the unit-cells become capacitive, and they support transverse electric (TE) wave propagation. On the other hand, the flow of TE and TM surface waves is suppressed near the resonance for a narrow band of frequencies, which is called the frequency band gap. In this band gap, the metasurfaces can behave as high impedance surfaces and can reflect a maximum number of waves with in-phase characteristics.

On the other hand, RCS is reduced by enhancing the gain and cancelling the interference caused by the reflected E-fields in various sections of the unit-cell array of the metasurface [32]. To understand the polarization conversion mechanism, Figure 1(e) is depicted, which indicates a reflection of a y-polarized wave upon the incident of an x-polarized wave or vice versa.

3. PERFORMANCE IMPROVEMENT USING METASURFACE

This section discusses the various performance improvements that include impedance bandwidth enhancement, gain enhancement, size reduction, SAR reduction, RCS reduction, and polarization conversion.

3.1. Bandwidth and Gain Enhancement

The present era of wireless communications necessitates a speedy and reliable transmission rate for the benefit of people's day-to-day activities. In addition, for multiple wireless networks to coexist, transceivers must simultaneously operate in multiple frequency bands. To simultaneously function in various frequency bands with a high and consistent transmission rate, a broad frequency band antenna is required. To obtain broader impedance-bandwidth, the authors of [33] utilized an artificial magnetic conductor (AMC) reflector below a CP radiator. The authors of [34] achieved broad impedance bandwidth using a nonuniform metasurface.

Gain improvement is also important since it extends the range of communications and improves the signal-to-noise ratio (SNR). High gains can be easily achieved using microstrip antennas, which are inherently advantageous due to their light weight, ease of fabrication, low cost, and conformability to various types of surfaces [35–39]. However, the impedance bandwidth provided by a microstrip antenna is narrow. Alternately, the PEC was frequently placed beneath the radiator at a distance of quarter wavelength [40]. However, the quarter wavelength separation for in-phase reflection increases the overall footprint. To overcome these issues, AMC was introduced, which behaved as a PMC and could reduce the antenna profile [41]. Scientists have also used parasitic and periodic structures above the main radiator to improve the gain. In [42], a parasitic patch was positioned above the main radiator in the direction of radiation, thereby increasing the electromagnetic field concentration. In advance of that, the authors of [43] used a dual-sided partially reflective surface (PRS) based on a self-complementary structure on the top of the radiator to enhance the gain. In [44], the proposed AMC enhanced the gain, and the orthogonal differentially fed radiators above the AMC providing high isolation. Because the majority of vehicle-mounted antennas offer either a broad bandwidth or a high gain at a time, it is quite challenging to develop antennas that function in many wireless communication bands of base stations and have both a broad bandwidth and a high gain. Therefore, a few researchers have worked on enhancing impedance bandwidth and gain. The authors of [45] have proposed a reconfigurable antenna using a dual band operated AMC in conjunction with PIN diodes. In advance of that, the authors of [46] have achieved wide impedance bandwidth with high gain by putting two dipole radiators in the shape of a bow-tie at right angles to each other and improving port isolation by giving them different polarizations. By producing additional resonance, the trapezoidal parasitic elements expanded the impedance bandwidth. The AMC of cylindrical types enhanced the gain. The structure of the proposed

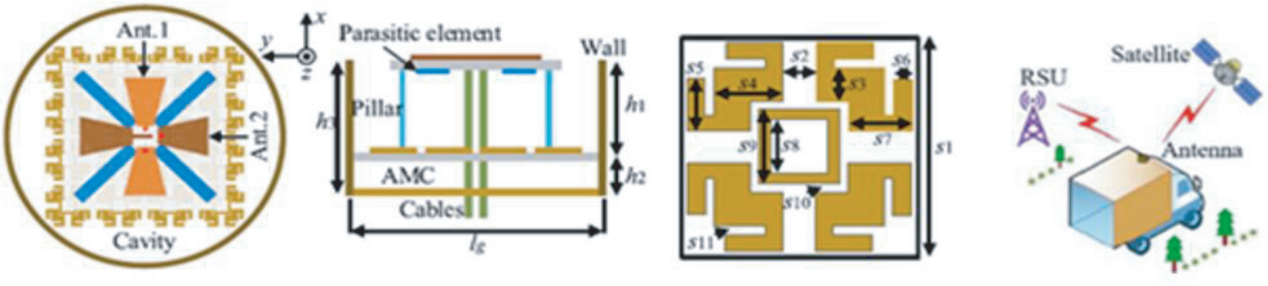

(a) (b) (c) (d)

Figure 2. Structure of (a) top-view of the antenna, (b) side-view of the antenna, (c) unit-cell of the AMC, and (d) antenna mounted on vehicle [46].

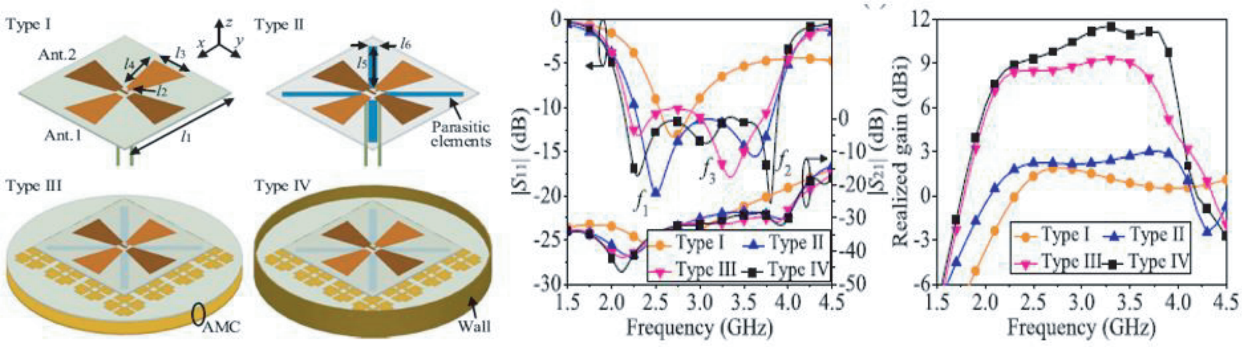

(a) (b) (c)

Figure 3. (a) Antenna evolution starting from Type I to Type IV. (b) Reflection coefficients. (c) Realized gain.

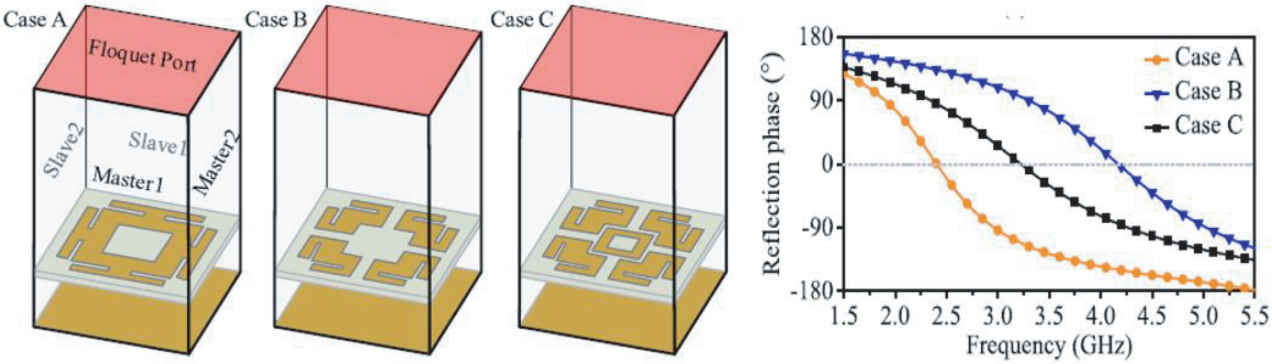

(a) (b)

Figure 4. (a) Unit-cell evolution, and (b) reflection-characteristics of the unit-cells.

wideband antenna is depicted in Figure 2. The proposed wideband antenna was based on the evolution-in-steps strategy, as depicted in Figure 3(a). Initially, Type-I was formed by arranging two similar types of dipoles orthogonally, and then by inserting four parasitic strips in between, Type-II was formed. Then the AMC was incorporated beneath Type-II which formed Type-III. Finally, the Type-III structure was covered by a metallic cylinder to form Type-IV. Reflection coefficient and realized gain of the above mentioned antennas are given in Figures 3(b) and (c), respectively. Figure 4(a) shows the evolution of the unit-cells of the AMC. In the first step, Case-A consists of a square-ring-type unit-cell attached with four T-shaped metallic patches. Then in Case-B, the unit-cell was modified by etching rectangular slots. Finally, in Case-C, the unit-cell is modified by introducing square rings at the center. Figure 4(b) compares the reflection phases of Case-A, Case-B, and Case-C configurations. Figure 5 depicts the equivalent-circuit-model (ECM) of the optimized unit-cell using the theories presented in [47] in order to further comprehend the wideband working mechanism of Case C. The authors have also formulated bandwidth (BW) and resonant frequency (f_0) using the equations presented in [48] as follows:

$$BW = \frac{1}{\eta}\sqrt{\frac{(L_d \backslash\backslash L_p + L_{12})}{C_p + C_{12}}} \tag{8}$$

$$f_0 = \frac{1}{2\pi\sqrt{(L_d \backslash\backslash L_p + L_{12})(C_p + C_{12})}} \tag{9}$$

$$C_p = C_1 + \frac{C_2 C_4}{C_2 + C_4} + C_3 \tag{10}$$

$$L_p = L_1 \backslash\backslash (L_2 + L_4) \tag{11}$$

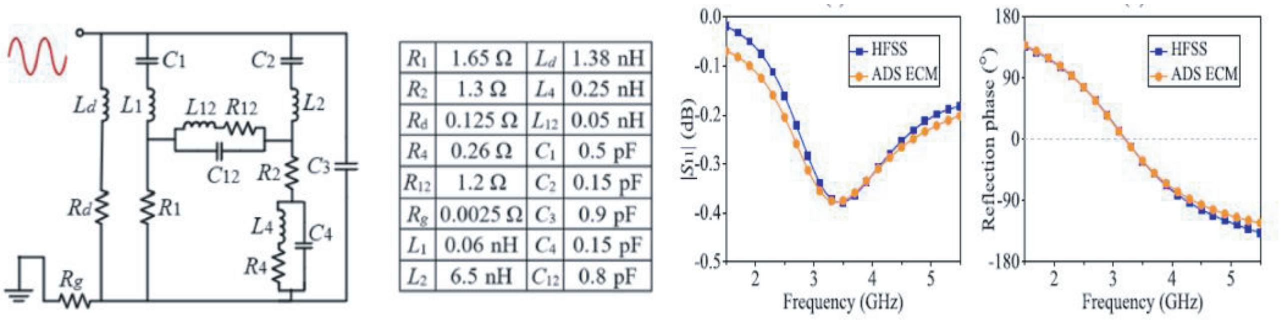

R_1	1.65 Ω	L_d	1.38 nH
R_2	1.3 Ω	L_4	0.25 nH
R_d	0.125 Ω	L_{12}	0.05 nH
R_4	0.26 Ω	C_1	0.5 pF
R_{12}	1.2 Ω	C_2	0.15 pF
R_g	0.0025 Ω	C_3	0.9 pF
L_1	0.06 nH	C_4	0.15 pF
L_2	6.5 nH	C_{12}	0.8 pF

(a) (b) (c) (d)

Figure 5. (a) Equivalent-circuit-model, and (b) obtained values of component, (c) reflection coefficients, and (d) reflection phase characteristics [47].

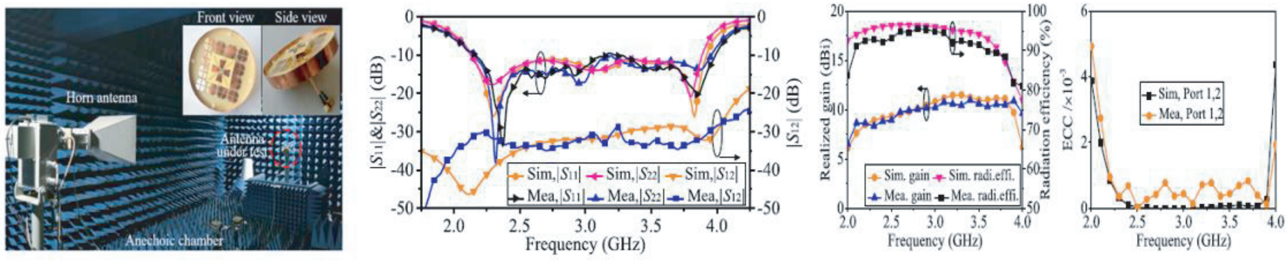

(a) (b) (c) (d)

Figure 6. (a) Fabricated prototype, (b) Measured reflection coefficients, (c) Measured gain and radiation efficiency, and (d) ECC [47].

where η, C_p, and L_p represent the free space impedance, self-capacitance, and self-inductance of the metallic unit-cells, respectively.

Figure 6 depicts the fabricated antenna and measured results. A low-profile antenna with a broad bandwidth and high gain has been presented [49]. Wide impedance bandwidth was achieved by producing two resonances using a bow-tie radiator for the first resonant frequency and a parasitic radiator for the second resonance. High gain was achieved using the cylindrical AMC cavity-backed structure. One of the authors of this article, Sahu, has worked on impedance bandwidth and gain enhancement by incorporating metasurfaces beneath a monopole antenna [24–27]. Table 1 summarizes the enhanced gain and impedance bandwidth of the existing literature.

Table 1. Enhanced gain by the literatures.

Ref.	f_r (GHz)	FBW (%)	Height	Realized Gain (dB)	Isolation (dB)	Efficiency (%)	Types of Reflector
[34]	7.5	57.76	$0.5\lambda_0$	< 12.5	NA	44	PRS
[41]	2.68	22.3	$0.074\lambda_0$	< 7	28	83.5	AMC
[33]	2.26	54.8	$0.134\lambda_0$	6.6–8	25	82	AMC
[49]	2.66	22	$0.134\lambda_0$	9–9.3	40	82	PEC
[50]	2.08	64.7	$0.534\lambda_0$	7.9–9.1	26	NA	PEC
[51]	2.22	46.8	$0.254\lambda_0$	5.8–8.5	40	NA	PEC
[52]	3.55	31.0	$0.194\lambda_0$	6.6–7.3	25	NA	AMC
[46]	3.06	58.82	$0.184\lambda_0$	8.34–10.96	28.65	88.6	AMC

3.2. Miniaturization

As essential as wide-bandwidth and high-gain antennas are, electrically small antennas (ESAs) have generated a great deal of interest for the use in day-to-day accessories due to their compactness. Nevertheless, ESA [53, 54] generally offers low efficiency and a limited bandwidth. To overcome these problems, metasurfaces are extensively used to achieve miniaturization with high efficiency and a wider impedance bandwidth due to their unusual EM properties, such as negative permittivity and permeability. A metamaterial-based ESA with adequate radiation properties and isolation enhancement has been proposed in [55]. In order to further enhance performance, rectangular patches are positioned beneath a complementary split-ring resonator (CSRR) as shown in Figure 7, which is fixed in a small monopole with a size of $0.125\lambda_0$. The antenna was designed to operate tri-bands that cover the frequency ranges 2.4 to 2.5 GHz, 2.9 to 4.8 GHz, and 5.1 to 6.5 GHz. Furthermore, the authors have suggested a methodical, metamaterial-based strategy to enhance the isolation between two of these small, tightly spaced antenna elements at the lowest and highest frequency bands. Because they are small and tightly packed, the antennas can be easily incorporated into modern, compact communication devices with cutting-edge capabilities. Then, in [56], a high-gain miniaturized Antipodal Vivaldi Antenna (AVA) based on metasurface was reported for 24.75–27.5 and 27.5–28.35 GHz frequency bands for millimeter-wave communications in the upcoming 5G network. Figure 8 depicts the reported metasurface, which consists of an AVA array containing six two-stub-loaded split-ring resonators. The high value of $\varepsilon_{eff} \times \mu_{eff}$ provided by the metasurface (MS) is well-suited for antenna miniaturization design. After that, the authors of [57] investigated a dipole antenna surrounded by a metaresonator, which aids in antenna miniaturization. In [58], compactness was achieved by placing different electrically small monopoles close to split-ring and electric-LC resonators, respectively. The authors of [59] proposed a small tri-band monopole with single-cell metamaterial loading and a defective ground structure.

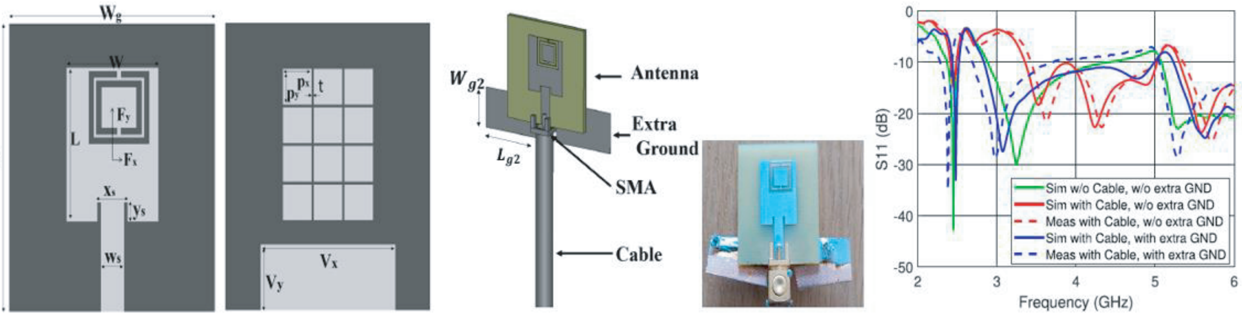

(a) (b) (c)

Figure 7. (a) ESAs (top & bottom view). (b) Simulated and fabricated antenna prototype. (c) Simulated and measured S_{11} [55].

It is important to note that in order to accomplish miniaturization, metaresonator-based antennas rely primarily on the interaction between the metaresonator and radiator, as opposed to relying solely on the negative permittivity or permeability metamaterial properties [58]. The dimensions of the antennas were significantly reduced, and the designs were astonishingly compact in relation to the wavelength in a number of works. Due to their limitations, ESAs'design is difficult and demands trade-offs between their size and performance. The primary difficulties persist despite the fact that metasurface has been successful in reducing the size of the antenna by enabling zero-order resonance [61]. For instance, the bandwidth of small metaresonator antennas is directly impacted by the narrowband nature of the metasurface. Furthermore, the majority of the designs primarily concentrated on reducing the size by enabling the subwavelength resonance of the metasurface without improving the overall performance of the integrated antenna. Furthermore, the interaction between the metasurface and the structure used to excite it was ignored even though the altered current-distribution degrades the overall performances. A simple ESA can be easily designed using a met resonator while achieving satisfactory performances caused by feeding, unit-cell metasurface location, shape of the antenna surface, etc. Therefore, more

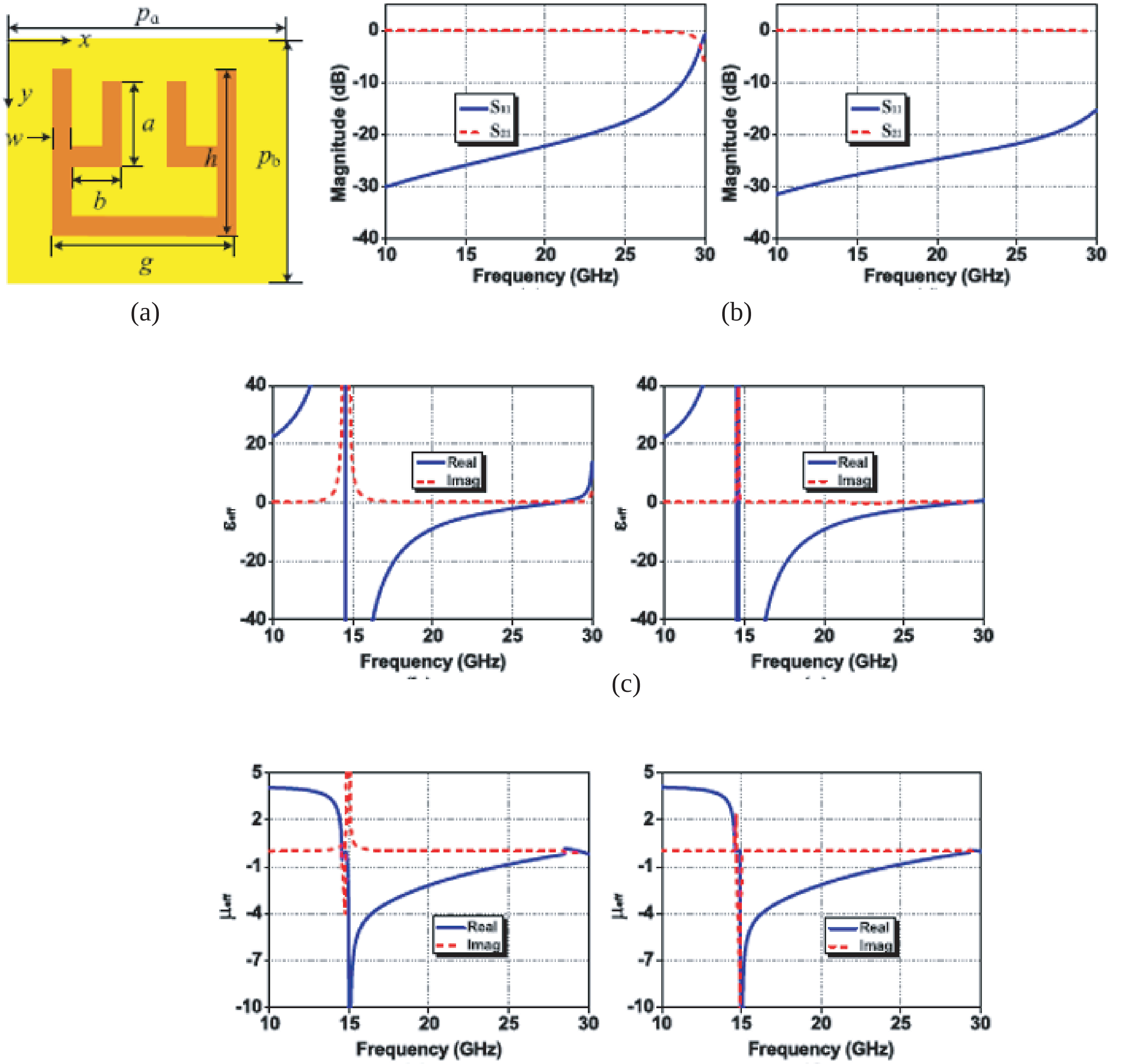

(a) (b)

(c)

(d)

Figure 8. (a) Schematic of the MS cell, (b) S-parameters under x & y polarization, (c) effective permittivity under x & y polarization and (d) effective permeability under x & y polarization [66].

research is required towards the size reduction of antennas using metasurface.

One of the authors of this article, Sahu, has worked on miniaturization by introducing rectangular slots and slits on the unit-cell of the proposed metasurface in [24] and rectangular slots on the unit-cell of the metasurface in [25–27]. Table 2 summarizes some of the existing ESAs.

3.3. SAR Reduction

An antenna used in a wearable application must meet certain criteria, including compact size, flexibility, high efficiency, and most importantly, minimal back radiation toward the human body. The fact is that, when an antenna operates close to the body, the backward radiation is absorbed by the human body,

Table 2. Miniaturized dimensions by the literatures.

Ref.	Size	Eff. (%)	BW (%)
[60]	$0.1\lambda \times 0.1\lambda$	90	4.9
[63]	$0.1\lambda \times 0.1\lambda$	28.1	0.4
[64]	$0.12\lambda \times 0.15\lambda$	29	2
[65]	$0.076\lambda \times 0.047\lambda$	64	3.6
[66]	$0.17\lambda \times 0.1\lambda$	98	2.4
[61]	$0.15\lambda \times 0.15\lambda$	55	1.55
[62]	$0.125\lambda \times 0.1\lambda$	60	4.1

and the antenna's performance is also degraded. The minimal back radiation helps reduce SAR to a safe level, which reduces the unwanted body effects caused by radiation [24–27]. SAR is the term for the parameter that indicates the amount of radiation absorbed by human body. The SAR is given by [27]

$$SAR = \frac{\sigma |E|^2}{\rho} \tag{12}$$

where σ represents the conductivity of human tissue, E the electric field, and ρ the mass density of human tissue.

Mainly PEC-based antennas [67], microstrip antennas [35], and metasurface based monopole antennas [24–27] have been used to obtain low SAR. However, the first one provides large footprints, and the second one provides a narrow impedance bandwidth. In contrast, the metasurface-based monopole antennas overcome these issues. The metasurface is used to isolate the monopole antenna from the human body. They provide in-phase reflection characteristics at resonant frequencies, which causes a reduction in the amount of back radiation, which in turn weakens the surface waves and increases the realized gain of the wearable antenna [68, 69]. To achieve low SAR, and high gain with a more compact structure, the researcher also developed metamaterial based antenna using composite right/left handed (CRLH) transmission line (TL) theory. The authors of [70] have proposed a CRLH-based radiator as shown in Figure 9(a) to produce zeroth-order resonance (ZOR) at 2.45 GHz. The designed antenna was tested against a human hand modelled in Computer Simulation Technology (CST), with a gap separation of 5 mm. As an AMC array structure supports the CRLH-radiator, there is hardly any impact from the human hand on the integrated design. As shown in Figure 9(b), the integrated design maintains the single band resonance at 2.45 GHz, with strong matching of −17 dB for the simulated result (black solid) and −12 dB for the measured one (red dotted).

In [71], an AMC-based dual-band diamond-shaped patch antenna was proposed that operated in the 1.575 GHz band with an impedance bandwidth of 1.84% and the 2.45 GHz band with an impedance

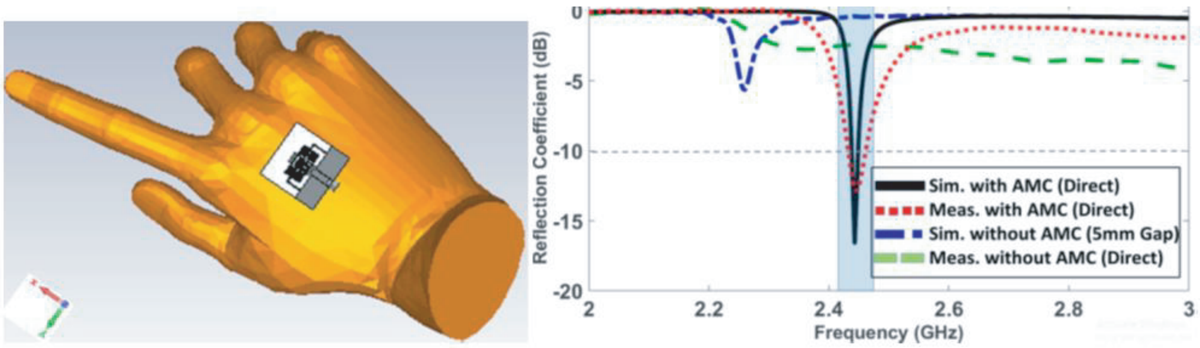

(a) (b)

Figure 9. (a) On-body CRLH antenna, and (b) simulated and measured reflection coefficients [70].

bandwidth of 0.73% for wearable applications. The suggested antenna was printed on semi-flexible Roger 3003C with a length × width of $1.85\lambda_g \times 1.85\lambda_g$ and 3.04 mm thickness, which is quite large in size. Furthermore, the obtained impedance bandwidth was very narrow. Another dual-band antenna supported by AMC that operated for wearable applications at 0.86 GHz and 2.4 GHz was described in [72]. After that, to achieve a low SAR with a more compact structure, the authors of [73] proposed an AMC-backed antenna for health monitoring using a polyimide substrate with a length × width of $0.09\lambda_g \times 0.09\lambda_g$ and thickness of 0.15 mm. The reported antenna provided an impedance bandwidth of 4.08% in the 2.45 GHz band and 2.24% in the 5.8 GHz band. Sahu, one of the authors of this article, has worked on lowering SAR by putting metasurfaces under the monopole antenna [24–27]. Table 3 summarizes some of the metasurface-based antennas used for on-body and off-body applications.

Table 3. Reduced SAR by the literatures.

Ref.	Type of Metasurface	Realized Gain (dB)	Efficiency (%)	SAR (W/kg)
[70]	AMC	6.51	74.8	0.22
[74]	EBG	7.8	N/A	0.0368
[75]	AMC	N/A	44	0.86
[76]	AMC	8.4	66	.33
[77]	EBG	N/A	N/A	0.554
[78]	AMC	5.2	61.3	2.48
[79]	EBG	7.93	N/A	0.07

3.4. RCS Reduction

RCS reduction has drawn interest from all around the world due to the significance of low scattering properties in contemporary warfare. The stealth capabilities of military systems have drawn a lot of interest due to the quick advancements in information technology and radar detection technologies. RCS is typically used to measure the stealth performance of a radar target; a lower RCS indicates higher stealth performance. Shape optimization [80, 81] and microwave absorbing materials [82] are examples of traditional scattering suppression techniques. However, these methods either damage the antenna's morphological structure or are cumbersome, which makes them unsuitable for the use in actual situations. Due to their superior electromagnetic (EM) wave control, metasurfaces are now frequently used in the RCS reduction of targets [83]. In [84], a hybrid structure made up of a band-pass frequency selective surface (FSS) is used to replace the antenna array's ground. Apart from that, researchers have worked on wideband RCS reduction through interference cancellation from reflected E-fields in various polarization conversion metasurface (PCM) array sections. An F-P cavity is built in [85] using an FSS superstrate and the antenna ground. In the meantime, there is a 180° variation in the reflection phase between the FSS superstrate's metal patch-containing and -free portions. The antenna array's RCS is reduced as a result of the interference cancellation of the reflected E-fields. In [32], a PCM antenna array with low RCS along with CP characteristics was suggested. The interference cancellation of the reflected electric fields between adjacent antenna units is made possible by the checkerboard design of the antenna units. The authors in [86] suggested a split-ring-resonator (SRR)-based metasurface that, when incorporated with a monopole antenna, reduced the RCS and enhanced the gain, as shown in Figure 10. The metasurface was formed with the arrangement of four 2 × 2 arrayed SRRs, where each array was orthogonal to the other. Such arrangement was adopted to achieve CP characteristics.

In [87], the authors have incorporated a new coding metasurface (CM) into a microstrip antenna array (MAA) that reduces RCS for a wide frequency range without disturbing radiation properties. The metasurface has a low Q value, which controls the phases of the reflected wave for a wide band of frequencies. Additionally, the convolution theorem-based quick optimization technique is suggested, which improves the coding matrix's optimization effectiveness. Finally, the MAA is applied to the CM for wideband RCS reduction using two different types of low Q resonators. According to the measured

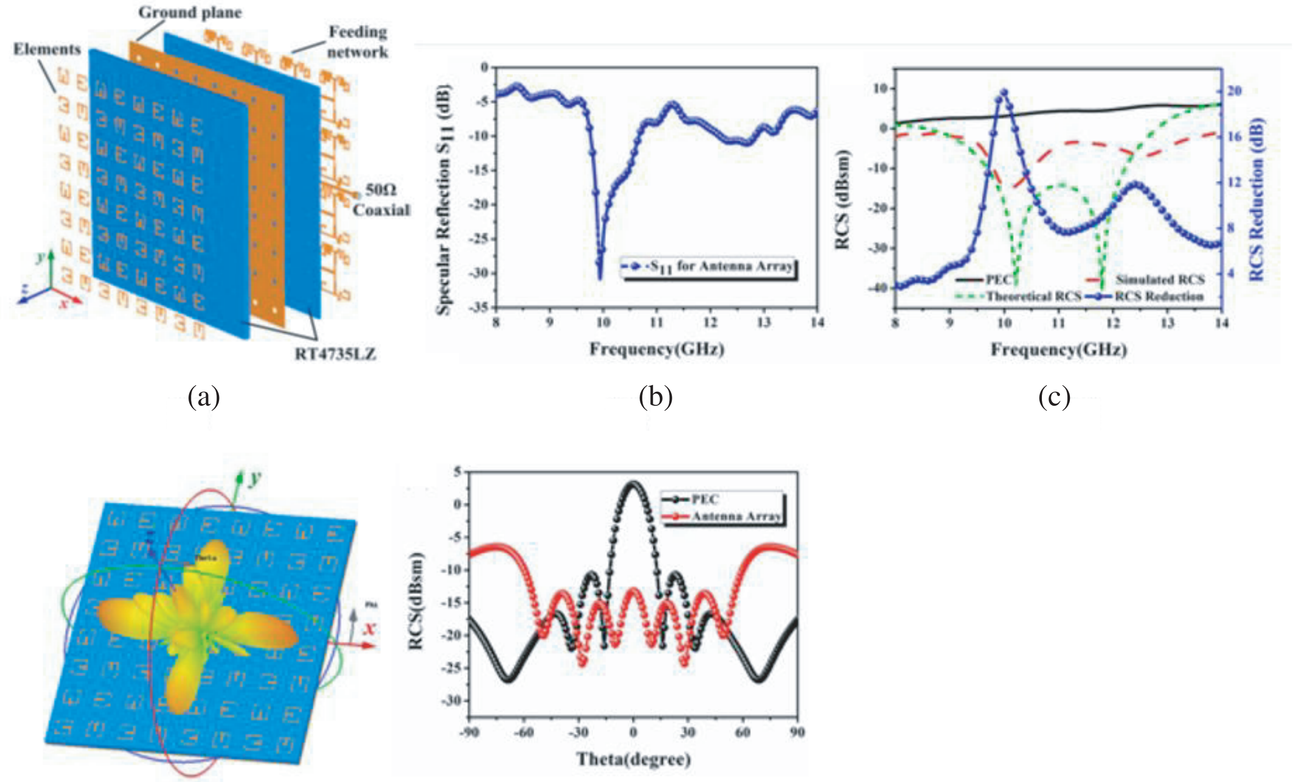

(a) (b) (c)

(d) (e)

Figure 10. (a) Structure of the LCP-MA, (b) specular-reflection-coefficients, (c) RCS characteristics, (d) 3-D radiation pattern, and (e) RCS characteristics [86].

results, the suggested low RCS MAA (LRMAA) may achieve more than 10 dB RCS reduction in the 5.8–21.5 GHz frequency range, showing better specular scattering suppression. In parallel, the LRMAA's radiation characteristics match those of MAA. The suggested method successfully integrates radiation and scattering characteristics, which could be useful for antenna systems on stealth devices. Table 4 summarizes the results of recent work regarding reduced SAR by the literatures.

Table 4. Reduced RCS by the literatures.

Ref.	Bandwidth (%)	10 dB Monostatic RCS Reduction BW	Periodicity of Unit-cell	Antenna Gain loss with/without Metasurface
[87]	29.52	5.8–21.5 GHz/115.02%	$.12\lambda_0$ @ 5.8 GHz	−0.7 dB
[88]	12.37	6.2–27.3 GHz/126% @5 dB	$.12\lambda_0$ @ 6.2 GHz	N/A
[89]	11.61	3–4.3 GHz/35.62% @5 dB	$.3\lambda_0$ @ 3 GHz	−2 dB
[90]	6.56	9.5–11.5 GHz/19.05%	$.29\lambda_0$ @ 9.5 GHz	N/A
[91]	6.95	7.65–9.8 GHz/24.64%	$.4\lambda_0$ @ 7.65 GHz	< 1 dB
[92]	19.67	28–48 GHz/52.63%	$.33\lambda_0$ @ 7 GHz	10 dB enhanced

3.5. Polarization Conversion

In the modern era of communications, the polarization conversion plays an important role due to its wide application in the field of contrast imaging microscopy, optical sensing, molecular biotechnology, and microwave communication. The polarization conversion mainly indicates the cross polarization conversion [93], linear-to-circular conversion [94], and circular-to-linear conversion [95]. As such, polarization conversion metasurface (PCMS) is widely used for polarization conversion applications due to its ability to control and manipulate the EM wave [93–95]. In this regard, the researchers have attempted to enhance the conversion bandwidth by proposing wideband cross-polarization-converting metasurfaces [96] and to achieve polarization conversions in multi-bands by proposing multi-bands operated reflecting PCMSs [97, 98]. The polarization conversion properties are accessed by polarization conversion ratio (PCR), and the overall effectiveness of energy conversion is measured by the energy conversion ratio (ECR) and can be defined as [99]

$$PCR = \frac{r_{xy}^2}{r_{xy}^2 + r_{yy}^2} \quad \& \quad ECR = \frac{|E_x^r|^2 + |E_y^r|^2}{|E_y^i|^2} = r_{xx}^2 + r_{yy}^2 \tag{13}$$

$$r_{xy} = \frac{|E_x^r|}{|E_y^i|} \quad \& \quad r_{yy} = \frac{|E_y^r|}{|E_y^i|} \tag{14}$$

where r_{xy} and r_{yy} denote the cross- and co-polarized reflection coefficients, respectively with y-polarized incident electric field (E_y^i) and x-polarized reflected electric field (E_x^r).

In addition to the above literature where polarization conversion characteristics using PCMSs have been focused, the authors of [100–104, 25] have worked on improving the antenna's performance using the PCMS. In [101], a polarization rotation artificial magnetic conductor (PRAMC) was proposed to achieve dual CP characteristics by incidenting LP waves from a dual band monopole antenna on it, as shown in Figure 11. Left-hand-circular-polarization (LHCP) was achieved in the lower band, which is 3.5 GHz, and right-hand-circular-polarization (RHCP) was achieved in the higher band, which is 5.8 GHz, with high gain and low backward radiation in each band. To demonstrate the polarization rotation mechanism, the authors have reported the relation between the reflected electric field ($\overrightarrow{E_r}$) and the incident electric field ($\overrightarrow{E_i}$) using the dyadic reflection coefficient ($\overline{\overline{\Gamma}}$) as follows

$$\overrightarrow{E_r} = \overline{\overline{\Gamma}} \times \overrightarrow{E_i} \tag{15}$$

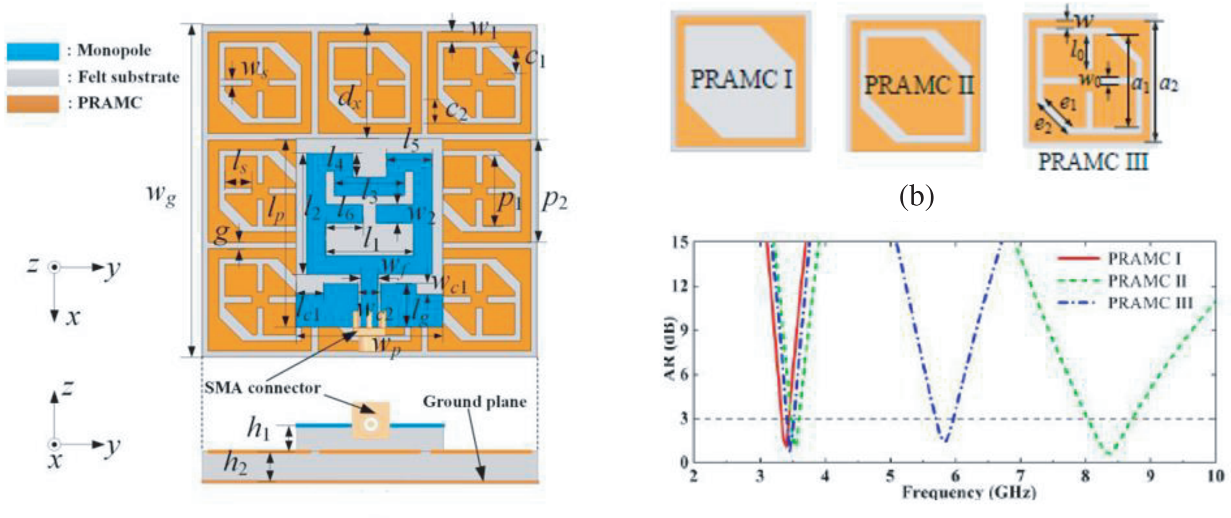

(a) (b) (c)

Figure 11. (a) Structure of PRAMC based antenna. (b) Evolution of PRAMC. (c) AR of Different PRAMC [101].

$$\overline{\overline{\Gamma}} = \begin{pmatrix} \Gamma_{x/x} & \Gamma_{x/y} \\ \Gamma_{y/x} & \Gamma_{y/y} \end{pmatrix} \tag{16}$$

where the subscript x/y represents the ratio of the x-component of reflected electric field to the y-component of incident electric field.

In [102], the authors have presented a wideband circularly polarized patch antenna inspired by an S-shaped metasurface for C-band applications as shown in Figure 12. As shown in Figure 12(c), the upper layer contains 4×4 periodic S-shaped metasurface elements; the middle layer contains a rectangular slotted ground plane; and the lower layer contains a coplanar waveguide (CPW)-fed microstrip structure. The coupling between the rectangular slot on the middle substrate and the CPW microstrip on the lower substrate created a linear polarized (LP) wave in the direction of electric field (E) along the Y-axis, and when the same field made contact with the 4×4 periodic S-shaped metasurface elements, it diverged into two orthogonal electric fields (E_1 and E_2) as shown in Figure 12(d).

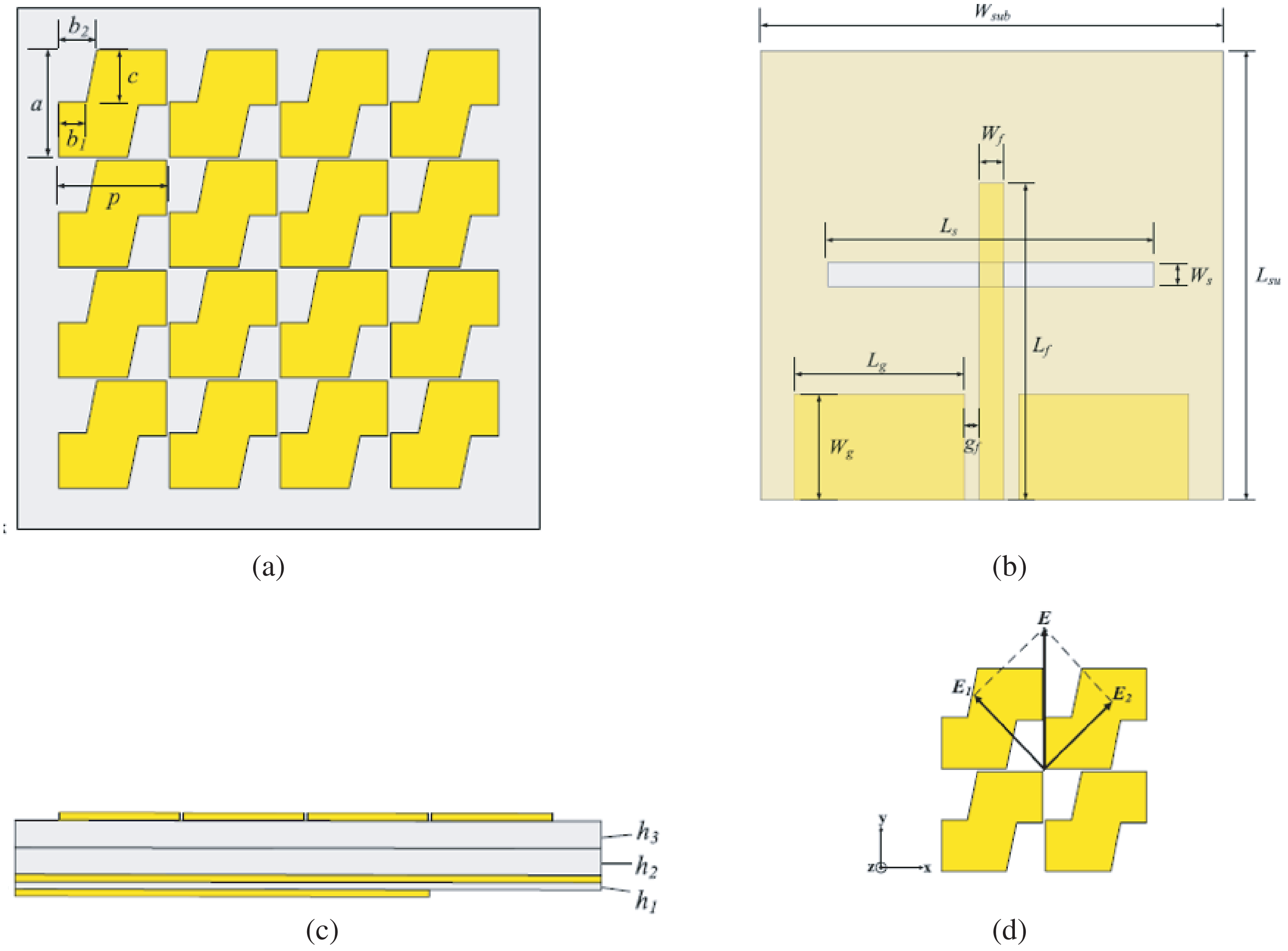

(a) (b)

(c) (d)

Figure 12. (a) Structure of S-shaped metasurface, (b) CPW-fed microstrip antenna, (c) S-shaped metasurface based antenna, and (d) electric-field orientation on the metasurface [102].

One of the authors of this article, Sahu, has worked on x-to-y polarization conversion at dual-band operation to achieve different states of polarization that include LHCP and RHCP [25]. Table 5 is presented to summarize the results of recent work regarding polarization converting metasurfaces.

Table 5. Metasurface used for polarization conversion by the existing literature.

Ref.	f_r (GHz)	Polarization	Types of Metasurface
[100]	5.6	LP/CP	Square cornered cut AMC
[101]	3.5/5.8	CP/CP	PRAMC
[102]	5.9	LP/CP	S-shaped MS
[103]	5.8	LP/CP	corner-truncated square MS
[104]	5.8	LP/CP	Square MS

4. PROPOSED DESIGN WITH RESULTS AND DISCUSSION

This section presents the design and discussion of developed metasurfaces to analyse the performance improvements by adopting the theories presented in Section 2. To design the proposed metasurfaces, initially, CRUC is designed theoretically at 2.45 GHz as shown in Figure 13(a), using the transmission line model adopted in [24, 25]. Using Equation (7), inductance 'L' is calculated as 3.77 nH for a substrate height of 3 mm. A felt material with a dielectric constant of 1.6 and a loss tangent of 0.044 is chosen as the substrate. The reason for choosing a felt substrate is to attain flexibility in body-worn applications. Then, 'C' is calculated as 1.12 pF using Equation (3) at 2.45 GHz. Following that, the size of the unit-cell (W) is calculated as nearly 35 mm with the gap (g) as 1.5 mm using Equation (5). Figure 13(b) shows the theoretical reflection phase characteristic, which is plotted using Equations (1) and (2). Then,

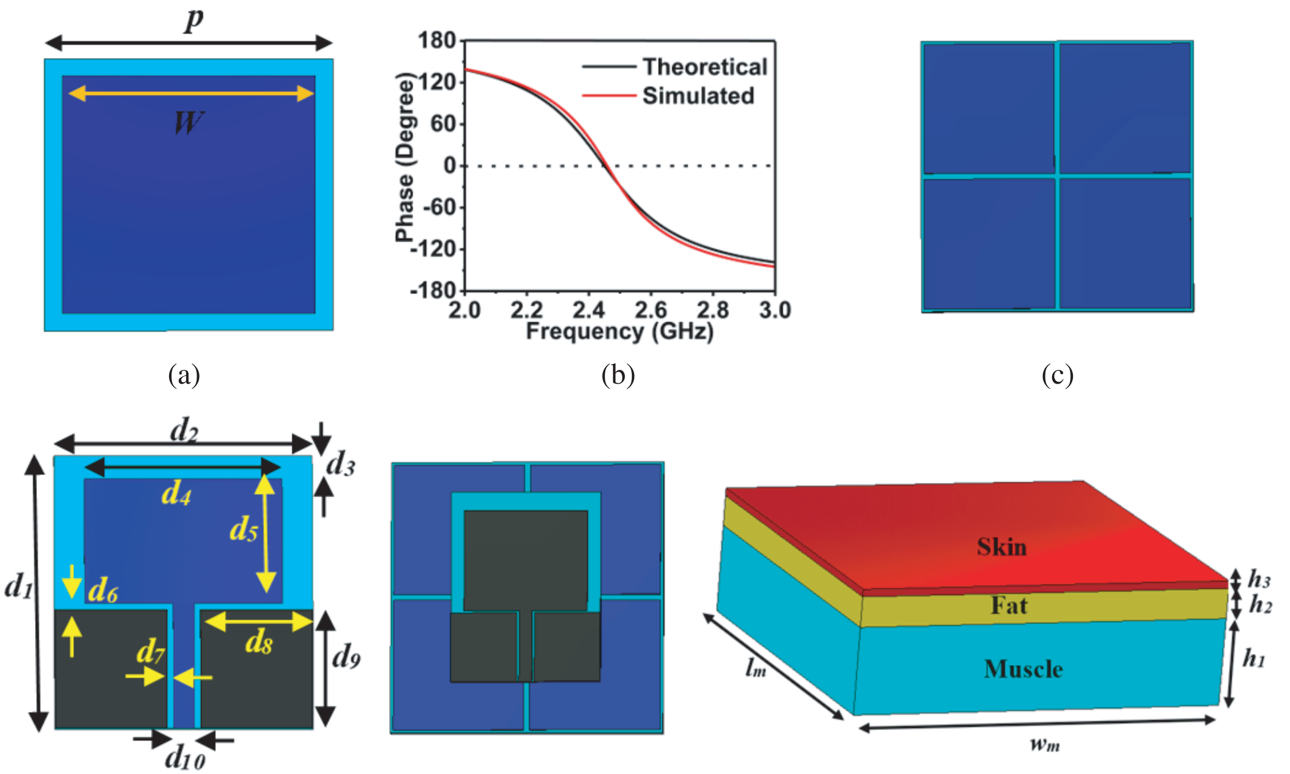

(a) (b) (c)

(d) (e) (f)

Figure 13. (a) Structure of CRUC, (b) theoretical vs simulated CRUC, (c) structure of CRUC based metasurface, (d) structure of MA ($d_1 = 51$ mm, $d_2 = 40$ mm, $d_3 = 5$ mm, $d_4 = 33$ mm, $d_5 = 27$ mm, $d_6 = 0.5$ mm, $d_7 = 0.6$ mm, $d_8 = 17.65$ mm, $d_9 = 18.5$ mm, and $d_{10} = 3.5$ mm), (e) structure of MSBMA, and (f) structure of RHBM ($h_1 = 23$ mm, $h_2 = 8$ mm, $h_3 = 2$ mm, $l_m = 100$ mm, and $w_m = 100$ mm).

the theoretically estimated unit-cell is simulated in CST Microwave Studio by setting the boundary as a unit-cell and the port as a Floquet port. The simulated reflection phase characteristic is shown in Figure 13(b), which possesses a 0° reflection phase at 2.47 GHz and is in good agreement with the theoretically estimated reflection phase characteristic.

To analyze the gain and impedance bandwidth enhancement, a 2×2 array of metasurface is designed by arranging CRUC in a periodic manner as shown in Figure 13(c). Then the designed metasurface (MS) is incorporated with a monopole antenna (MA), as depicted in Figure 13(d). The CPW-fed monopole radiator is printed on a felt substrate of 3 mm in height with a dielectric constant of 1.6 and a loss tangent of 0.044. Figure 13(e) shows the structure of a metasurface-based monopole antenna (MSBMA). Figure 14 shows the reflection coefficients, realized gain, and radiation efficiencies of the MA and MSBMA, with summaries of their results in Table 6.

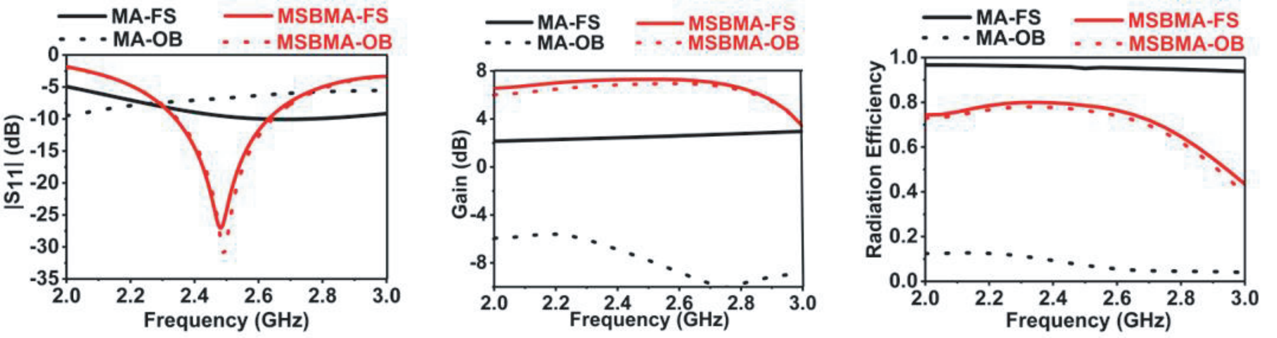

(a) (b) (c)

Figure 14. Performances of MA and MSBMA in Free Space (FS) and On-body (OB). (a) Reflection coefficients, (b) gain, and (c) radiation efficiency.

Table 6. Antenna performances in free space and on-body.

Antenna	Bandwidth (MHz) FS/OB	Gain (dB) FS/OB	Efficiency FS/OB	SAR (W/kg) 1 g/10 g
MA	140/Degraded	2.5/Degraded	0.95/Degraded	−0.7 dB
MSBMA	320/320	6.96/7.4	0.79/0.78	10 dB enhanced

To analyze body effects, SAR reduction, and other performances due to the presence of a metasurface, both MA and MSBMA are placed on a rectangular-human-body-model (RHBM) as shown in Figure 13(f). The RHBM is composed of a skin layer, a muscle layer, and a fat layer. The electrical properties and their thicknesses are tabulated in Table 7. Figure 14 shows the impedance bandwidth, realized gain, and radiation efficiencies in free space and on the body. The SAR distributions are evaluated over 1 g and 10 g standard with input power of 0.1 W for both MA and MSBMA, as shown in Figure 15. The free space and on-body performances with SAR values of both MA and MSBMA are summarized in Table 6.

Table 7. Properties of RHBM at 2.45 GHz [15].

LAYERS	Thickness (mm)	Permittivity	Conductivity (S/m)	Mass Densities (kg/m^3)
Skin	2	38.007	1.4640	1090
Fat	8	5.280	0.1045	930
Muscle	23	52.729	1.7388	1050

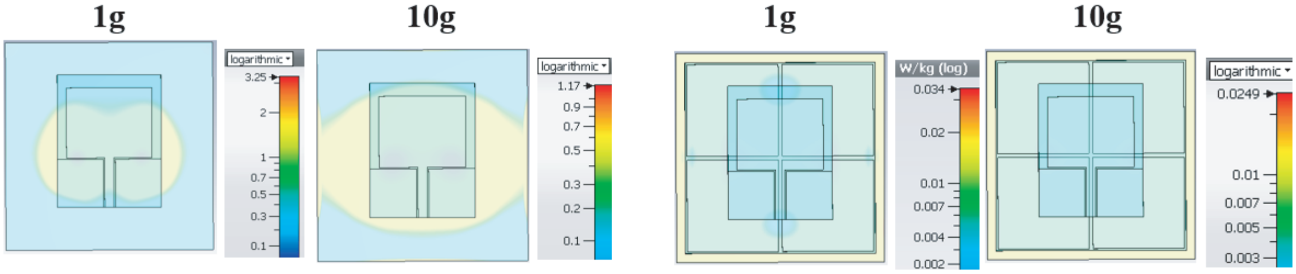

(a) (b)

Figure 15. 1 g and 10 g SAR distribution of (a) MA, and (b) MSBMA.

5. CONCLUSION

This review article presents the advancement of metasurface for antenna performance improvements that include impedance bandwidth, gain, size, SAR, RCS, and polarisation conversions. For each performance improvement, a theoretical perspective has been deduced. By adopting the discussed theories, MSBMA is developed to operate in the 2.45 GHz ISM band, which analyses impedance bandwidth enhancement, gain enhancement, and SAR reduction. The proposed monopole antenna, in the absence of the metasurface, provided an impedance bandwidth of 140 MHz and a gain of 2.5 dB. On the body, its performances degraded with a high value of SAR of 3.25 W/kg in 1 g standard and 1.17 W/kg in 10 g standard. On the other hand, the MSBMA increased the impedance bandwidth to 320 MHz and the gain to 7.4 dB. On the body, the performance of the MSBMA remains the same as free space, with a SAR reduction of 98.96% for 1 g of standard and 97.95% for 10 g of standard. Consequently, the use of metasurface in microwave and wireless technologies has resolved numerous problems while overcoming the limitations of conventional antenna designs.

REFERENCES

1. Tariq, F., M. R. A. Khandaker, K. K. Wong, M. A. Imran, M. Bennis, and M. Debbah, “A speculative study on 6G,” *IEEE Wireless Communications*, Vol. 27, No. 4, 118–125, 2020.
2. Almohammed, B., A. Ismail, and A. Sali, “Electro-textile wearable antennas in wireless body area networks: materials, antenna design, manufacturing techniques, and human body consideration — A review,” *Textile Research Journal*, Vol. 91, No. 5/6, 646–663, 2021.
3. Frezza, F., L. Pajewski, and G. Schettini, “Fractal two-dimensional electromagnetic bandgap structures,” *IEEE Transactions on Microwave Theory and Techniques*, Vol. 52, No. 1, 220–227, 2004.
4. Wang, L., L. Han, and W. Guo, “Hybrid Dirac semimetal-based photodetector with efficient low-energy photon harvesting,” *Light Sci. Appl.*, Vol. 11, 53, 2022.
5. Viti, L., A. Politano, K. Zhang, and M. S. Vitiello, “Thermoelectric terahertz photodetectors based on selenium-doped black phosphorus flakes,” *ESI for Nanoscale*, Vol. 4, 22–24, 2018.
6. Viti, L., J. Hu, D. Coquillat, et al., “Black phosphorus terahertz photodetectors,” *Adv. Materials*, Vol. 27, 5567–5572, 2015.
7. Xu. H., C. Guo, J. Zhang, et al., “PtTe2-based type-II dirac semimetal and its van der waals heterostructure for sensitive room temperature terahertz photodetection,” *Nano Micro. Small*, Vol. 15, 24–29, 2019.
8. Tang, W., A. Politano, and W. Guo, “Ultrasensitive room-temperature terahertz direct detection based on a bismuth selenide topological insulator,” *Advanced Functional Materials*, Vol. 28, No. 31, 1801786, 2018.

9. Liu, C., L. Wang, X. Chen, A. Politano, D. Wei, G. Chen, W. Tang, W. Lu, and A. Tredicucci, "Room-temperature high-gain long-wavelength photodetector via optical-electrical controlling of hot carriers in graphene," *Adv. Opt. Mater.*, Vol. 6, 22–28, 2018.
10. Viti, L., A. Politano, and M. S. Vitiello, "Black phosphorus nanodevices at terahertz frequencies: Photodetectors and future challenges," *APL Mater.*, Vol. 5, No. 3, 2017.
11. Viti, L., J. Hu, D. Coquillat, A. Politano, C. Consejo, W. Knap, and M. S. Vitiello, "Heterostructured hBN-BP-hBN nanodetectors at terahertz frequencies," *Advanced Materials*, Vol. 28, No. 34, 7390–7396, 2016.
12. Viti, L., D. Coquillat, and A. Politano, "Plasma-wave terahertz detection mediated by topological insulators surface states," *Nano Letters*, Vol. 16, No. 1, 80–87, 2016.
13. Rizza, C., D. Dutta, B. Ghosh, F. Alessandro, et al., "Extreme optical anisotropy in the type-II dirac semimetal NiTe2 for applications to nanophotonics," *ACS Applied Nano Materials*, Vol. 5, No. 12, 18531–18536, 2022.
14. Walser, R. M., A. Valanju, and P. W. Wins, "New smart materials for adaptive microwave signature control," *Proc. SPIE*, Vol. 3, 128–139, 1993.
15. Diaz, R. E. and S. A. Clavijo, "Artificial magnetic conductor," *Encyclopedia of RF and Microwave Engineering*, Chang K. C. ed., John Wiley & Sons, Inc., New York, 2005.
16. Yanghyo, K., F. Yang, and A. Elsherbeni, "Compact artificial magnetic conductor designs using planar square spiral geometries," *Progress In Electromagnetics Research*, Vol. 77, 43–54, 2007.
17. Li, L., Z. Wu, K. Li, et al., "Frequency-reconfigurable quasi-sierpinski antenna integrating with dual-band high-impedance surface," *IEEE Transactions on Antennas and Propagation*, Vol. 62, No. 9, 4459–4467, 2014.
18. Sievenpiper, D. F., "High-impedance electromagnetic surfaces. PhD dissertation," University of California, Los Angeles, 1999.
19. Liu, T., X. Y. Cao, J. J. Ma, and X. Wen, "Enhanced bandwidth uniplanar compact electromagnetic bandgap structure with coplanar meander line inductance," *Electronics Letters*, Vol. 44, 260–261, 2008.
20. Li, Y. Q., H. Zhang, Y.-Q. Fu, and N.-C. Yuan, "RCS reduction of ridged waveguide slot antenna array using EBG radar absorbing material," *IEEE Antennas and Wireless Propagation Letters*, Vol. 7, 473–476, 2008.
21. Dewan, R., M. K. A. Rahim, M. R. Hamid, et al., "Artificial magnetic conductor for various antenna applications: An overview," *Int. J. RF Microw. Comput. Aided Eng.*, Vol. 27, No. 6, 123–135, 2017.
22. Ashyap, A. Y. I., S. H. B. Dahlan, Z. Z. Abidin, et al., "An overview of electromagnetic band-gap integrated wearable antennas," *IEEE Access*, Vol. 8, 7641–7658, 2020.
23. Ashyap, A. Y. I., S. H. Dahlan, Z. Z. Abidin, et al., "Flexible antenna with HIS based on PDMS substrate for WBAN applications," *IEEE International RF and Microwave Conference (RFM)*, Vol. 3, 69–72, Penang, Malaysia, 2018.
24. Sahu, N. K. and S. K. Mishra, "Compact dual-band dual-polarized monopole antennas using via-free metasurfaces for off-body communications," *IEEE Antennas and Wireless Propagation Letters*, Vol. 21, No. 7, 1358–1362, 2022.
25. Sahu, N. K. and S. K. Mishra, "Polarization-converting metasurface inspired dual-band dual-circularly polarized monopole antennas for off-body communications," *IEEE Antennas and Wireless Propagation Letters*, Vol. 22, No. 1, 194–198, 2023.
26. Sahu, N. K. and S. K. Mishra, "A compact low SAR and high gain circularly polarized AMC integrated monopole antenna for WBAN applications," *Progress In Electromagnetics Research C*, Vol. 113, 211–226, 2021.
27. Sahu, N. K. and S. K. Mishra, "Anisotropic metasurface inspired circularly-polarized monopole antenna for OFF body communications," *IEEE Wireless Antenna and Microwave Symposium (WAMS)*, Vol. 1, 1–4, Rourkela, India, 2022.

28. Sievenpiper, D., L. Zhang, R. F. J. Broas, N. G. Alexopolous, and E. Yablonovitch, "High-impedance electromagnetic surfaces with a forbidden frequency band," *IEEE Transactions on Microwave Theory and Techniques*, Vol. 47, No. 11, 2059–2074, 1999.
29. Yang, F. and Y. Rahmat-Samii, "Reflection phase characterizations of the EBG ground plane for low profile wire antenna applications," *IEEE Transactions on Antennas and Propagation*, Vol. 51, No. 10, 2691–2703, 2003.
30. Mosallaei, H. and K. Sarabandi, "Antenna miniaturization and bandwidth enhancement using a reactive impedance substrate," *IEEE Transactions on Antennas and Propagation*, Vol. 52, No. 9, 2403–2414, 2004.
31. Goussetis, G., A. P. Feresidis, and J. C. Vardaxoglou, "Tailoring the AMC and EBG characteristics of periodic metallic arrays printed on grounded dielectric substrate," *IEEE Transactions on Antennas and Propagation*, Vol. 54, No. 1, 82–89, 2006.
32. Zhang, W., Y. Liu, and Y. Jia, "Circularly polarized antenna array with low RCS using metasurface-inspired antenna units," *IEEE Antennas and Wireless Propagation Letters*, Vol. 18, No. 7, 1453–1457, 2019.
33. Alshrafi, W., V. Ekaterinichev, and D. Heberling, "Wideband crossed dipoles antenna for all GNSS bands using wideband AMC," *Proc. 12th Eur. Conf. Antennas Propag.*, Vol. 2, 1–4, London, U.K., 2018.
34. Zhu, H., Y. Qiu, and G. Wei, "A broadband dual-polarized antenna with low profile using nonuniform metasurface," *IEEE Antennas and Wireless Propagation Letters*, Vol. 18, No. 6, 1134–1138, 2019.
35. Sahu, N. K. and S. K. Mishra, "Cavity model analysis of dual polarized microstrip antennas for wireless body area network application," *Int. J. Syst. Assur. Eng. Manag.*, 2022.
36. Sahu, N. K. and S. K. Mishra, "Analysis of omnidirectional antenna systems using cavity model," *IETE Journal of Research*, 2021.
37. Sahu, N. K. and A. K. Sharma, "The investigation on bandwidth enhancement of microstrip slot antennas," *Proc. of the Int. Conf. on Wireless Communication, Signal Processing And Networking, WISPNET*, Vol. 1. 953–956, 2016.
38. Sahu, N. K. and A. K. Sharma, "The investigation of pattern and frequency reconfigurable microstrip slot antenna using PIN diodes," *2017 Progress In Electromagnetics Research Symposium — Spring (PIERS)*, St. Petersburg, Russia, 2017.
39. Sahu, N. K. and A. K. Sharma, "A study on frequency reconfiguration of microstrip slot antenna using PIN diodes," *Proc. of the Int. Conf. on Communication System, Computing and IT Application, CSCITA*, 2017.
40. Chu, Q. X., D. L. Wen, and Y. Luo, "A broadband ±45° dual-polarized antenna with Y-shaped feeding lines," *IEEE Transactions on Antennas and Propagation*, Vol. 63, No. 2, 483–490, 2015.
41. Zhou, X., J. Shi, D. Feng, and H. Zhai, "A low-profile dual-polarized MIMO antenna array with high isolation," *2018 International Conference on Microwave and Millimeter Wave Technology (ICMMT)*, Vol. 1, 1–3, Chengdu, China, 2018.
42. Wang, W. and Y. Zheng, "Improved design of the Vivaldi dielectric notch radiator with etched slots and a parasitic patch," *IEEE Antennas and Wireless Propagation Letters*, Vol. 17, No. 6, 1064–1068, 2018.
43. Goudarzi, A., M. Movahhedi, M. M. Honari, H. Saghlatoon, R. Mirzavand, and P. Mousavi, "Wideband high-gain circularly polarized resonant cavity antenna with a thin complementary partially reflective surface," *IEEE Transactions on Antennas and Propagation*, Vol. 69, No. 1, 532–537, 2021.
44. Feng, B., X. He, J.-C. Cheng, Q. Zeng, and C.-Y.-D. Sim, "A low-profile differentially fed dual-polarized antenna with high gain and isolation for 5G microcell communications," *IEEE Transactions on Antennas and Propagation*, Vol. 68, No. 1, 90–99, 2020.
45. Nie, Z., H. Zhai, L. Liu, J. Li, D. Hu, and J. Shi, "A dual-polarized frequency-reconfigurable low-profile antenna with harmonic suppression for 5G application," *IEEE Antennas and Wireless Propagation Letters*, Vol. 18, No. 6, 1228–1232, 2019.

46. Yang, S., L. Liang, W. Wang, Z. Fang, and Y. Zheng, "Wideband gain enhancement of an AMC cavity-backed dual-polarized antenna," *IEEE Transactions on Vehicular Technology*, Vol. 70, No. 12, 12703–12712, 2021.
47. Wang, W., Y. Chen, S. Yang, X. Zheng, and Q. Cao, "Design of a broadband electromagnetic wave absorber using a metamaterial technology," *Journal of Electromagnetic Waves and Applications*, Vol. 29, No. 15, 2080–2091, 2015.
48. Shi, S., et al., "Wideband planar phased array antenna based on artificial magnetic conductor surface," *IEEE Transactions on Circuits and Systems II: Express Briefs*, Vol. 67, No. 10, 1909–1913, 2020.
49. Lee, J.-N., K.-C. Lee, and P.-J. Song, "The design of a dual-polarized small base station antenna with high isolation having a metallic cube," *IEEE Transactions on Antennas and Propagation*, Vol. 63, No. 2, 791–795, 2015.
50. Ye, L. H., X. Y. Zhang, Y. Gao, and Q. Xue, "Wideband dual-polarized four-folded-dipole antenna array with stable radiation pattern for base-station applications," *IEEE Transactions on Antennas and Propagation*, Vol. 68, No. 6, 4428–4436, 2020.
51. Cui, Y., Y. Niu, Y. Qin, and R. Li, "A new high-isolation broadband flush-mountable dual-polarized antenna," *IEEE Transactions on Antennas and Propagation*, Vol. 66, No. 12, 7342–7347, 2018.
52. Zhu, J., S. Li, S. Liao, and Q. Xue, "Wideband low-profile highly isolated MIMO antenna with artificial magnetic conductor," *IEEE Antennas and Wireless Propagation Letters*, Vol. 17, No. 3, 458–462, 2018.
53. Chu, L. J., "Physical limitations of omnidirectional antennas," *J. Appl. Phys.*, Vol. 19, 1163–1175, 1948.
54. Wheeler, H. A., "Fundamental limitations of small antennas," *Proc. IRE*, Vol. 35, 1479–1484, 1947.
55. Milias, C., R. B. Andersen, P. I. Lazaridis, et al., "Miniaturized multiband metamaterial antennas with dual-band isolation enhancement," *IEEE Access*, Vol. 10, 64952–64964, 2022.
56. Zhu, S., H. Liu, and P. Wen, "A new method for achieving miniaturization and gain enhancement of vivaldi antenna array based on anisotropic metasurface," *IEEE Transactions on Antennas and Propagation*, Vol. 67, No. 3, 1952–1956, 2019.
57. Ziolkowski, R. W. and A. Erentok, "Metamaterial-based efficient electrically small antennas," *IEEE Transactions on Antennas and Propagation*, Vol. 54, No. 7, 2113–2130, 2006.
58. Ntaikos, D. K., N. K. Bourgis, and T. V. Yioultsis, "Metamaterial-based electrically small multiband planar monopole antennas," *IEEE Antennas and Wireless Propagation Letters*, Vol. 10, 963–966, 2011.
59. Zhu, J., M. A. Antoniades, and G. V. Eleftheriades, "A compact tri-band monopole antenna with single-cell metamaterial loading," *IEEE Transactions on Antennas and Propagation*, Vol. 58, No. 4, 1031–1038, 2010.
60. Ntaikos, D. K., N. K. Bourgis, and T. V. Yioultsis, "Metamaterial-based electrically small multiband planar monopole antennas," *IEEE Antennas and Wireless Propagation Letters*, Vol. 10, 963–966, 2011.
61. Odabasi, H., F. L. Teixeira, and D. O. Guney, "Electrically small, complementary electric-field-coupled resonator antennas," *J. Appl. Phys.*, Vol. 113, No. 8, Art. No. 084903, 2013.
62. Milias, C., R. B. Andersen, P. I. Lazaridis, et al., "Miniaturized multiband metamaterial antennas with dual-band isolation enhancement," *IEEE Access*, Vol. 10, 64952–64964, 2022.
63. Ouedraogo, R. O., E. J. Rothwell, A. R. Diaz, K. Fuchi, and A. Temme, "Miniaturization of patch antennas using a metamaterial-inspired technique," *IEEE Transactions on Antennas and Propagation*, Vol. 60, No. 5, 2175–2182, 2012.
64. Sharawi, M. S., M. U. Khan, A. B. Numan, and D. N. Aloi, "A CSRR loaded MIMO antenna system for ISM band operation," *IEEE Transactions on Antennas and Propagation*, Vol. 61, No. 8, 4265–4274, 2013.

65. Zhu, J. and G. V. Eleftheriades, "Dual-band metamaterial-inspired small monopole antenna forWiFi applications," *Electron. Lett.*, Vol. 45, No. 22, 1104–1106, 2009.
66. Zhu, K., C. Li, L. Li, Y.-M. Cai, and C.-H. Liang, "Design of electrically small metamaterial antenna with ELC and EBG loading," *IEEE Antennas and Wireless Propagation Letters*, Vol. 12, 678–681, 2013.
67. Atrash, M. E., O. F. Abdalgalil, I. S. Mamoud, M. A. Abdallaand, and S. R. Zahran, "Wearable high gain low SAR antenna loaded with backed all-textile EBG for WBAN applications," *IET Microw. Antennas Propag.*, Vol. 14, No. 8, 791–799, 2020.
68. Ashyap, A. Y. I., et al., "Compact and low-profile textile EBG-based antenna for wearable medical applications," *IEEE Antennas and Wireless Propagation Letters*, Vol. 16, 2550–2553, 2017.
69. Alemaryeen, A. and S. Noghanian, "On-body low-profile textile antenna with artificial magnetic conductor," *IET Microw., Antennas Propag.*, Vol. 12, No. 4, 627–635. 2018.
70. Atrash, M. El, M. A. Abdalla, and H. M. Elhennawy, "A compact highly efficient Π-section CRLH antenna loaded with textile AMC for wireless body area network applications," *IEEE Transactions on Antennas and Propagation*, Vol. 69, No. 2, 648–657, 2021.
71. Paracha, K. N., S. K. A. Rahim, P. J. Soh, et al., "A low profile, dual-band, dual polarized antenna for indoor/outdoor wearable application," *IEEE Access*, Vol. 7, 33277–33288, 2019.
72. Chuquitarco-Jimenez, C. A., E. Antonino-Daviu, and M. Ferrando-Bataller, "Dual-band antenna with AMC for wearable applications," *Proc. 15th Eur. Conf. Antennas Propag. (EuCAP)*, 1–4, 2021.
73. Yin, B., M. Ye, Y. Yu, and J. Gu, "A dual-band, miniaturized, AMC-based wearable antenna for health monitoring applications," *Progress In Electromagnetics Research C*, Vol. 112, 165–177, 2021.
74. Ashyap, A. Y. I., Z. Z. Abidin, S. H. Dahlan, et al., "Compact and low-profile textile EBG-based antenna for wearable medical applications," *IEEE Antennas and Wireless Propagation Letters*, Vol. 16, 2550–2553, 2017.
75. Mersani, A., L. Osman, and J. M. Ribero, "Performance of dualband AMC antenna for wireless local area network applications," *IET Microw., Antennas Propag.*, Vol. 12, No. 6, 872–878, 2018.
76. Alemaryeen, A. and S. Noghanian, "Crumpling effects and specific absorption rates of flexible AMC integrated antennas," *IET Microw., Antennas Propag.*, Vol. 12, No. 4, 627–635, 2018.
77. Gao, G.-P., B. Hu, S.-F. Wang, and C. Yang, "Wearable circular ring slot antenna with EBG structure for wireless body area network," *IEEE Antennas and Wireless Propagation Letters*, Vol. 17, No. 3, 434–437, 2018.
78. Wang, M., Z. Yang, J. Wu, et al., "Investigation of SAR reduction using flexible antenna with metamaterial structure in wireless body area network," *IEEE Transactions on Antennas and Propagation*, Vol. 66, No. 6, 3076–3086, June 2018.
79. Abirami, B. S. and E. F. Sundarsingh, "EBG-backed flexible printed Yagi-Uda antenna for on-body communication," *IEEE Transactions on Antennas and Propagation*, Vol. 65, No. 7, 3762–3765, 2017.
80. Jiang, W., Y. Liu, S. Gong, and T. Hong, "Application of bionics in antenna radar cross section reduction," *IEEE Antennas and Wireless Propagation Letters*, Vol. 8, 1275–1278, 2009.
81. Wang, W., S. Gong, X. Wang, Y. Guan, and W. Jiang, "Differential evolution algorithm and method of moments for the design of low-RCS antenna," *IEEE Antennas and Wireless Propagation Letters*, Vol. 9, 295–298, 2010.
82. Pozar, D. M., "RCS reduction for a microstrip antenna using a normally biased ferrite substrate," *IEEE Microwave and Guided Wave Letters*, Vol. 2, No. 5, 196–198, 1992.
83. He, Q., S. Sun, S. Xiao, and L. Zhou, "High-efficiency metasurfaces: Principles, realizations, and applications," *Adv. Opt. Mater.*, Vol. 6, No. 19, 1–23, 2018.
84. Li, Y.-Q., H. Zhang, Y.-Q. Fu, and N.-C. Yuan, "RCS reduction of ridged waveguide slot antenna array using EBG radar absorbing material," *IEEE Antennas and Wireless Propagation Letters*, Vol. 7, 473–476, 2008.

85. Jia, Y. and Y. Liu, "Low-RCS and high-gain broadband circularly polarized antenna," *2017 IEEE International Symposium on Antennas and Propagation & USNC/URSI National Radio Science Meeting*, 1923–1924, San Diego, CA, USA, 2017.
86. Fan, Y., J. Wang, Y. Li, J. Zhang, Y. Han, and S. Qu, "Low-RCS and high-gain circularly polarized metasurface antenna," *IEEE Transactions on Antennas and Propagation*, Vol. 67, No. 12, 7197–7203, 2019.
87. Xi, Y., W. Jiang, K. Wei, T. Hong, T. Cheng, and S. Gong, "Wideband RCS reduction of microstrip antenna array using coding metasurface with low Q resonators and fast optimization method," *IEEE Antennas and Wireless Propagation Letters*, Vol. 21, No. 4, 656–660, 2022.
88. Kang, X., J. Su, H. Zhang, Z. Li, and Y. L. Yang, "Ultra-wideband RCS reduction of microstrip antenna array by optimized multi-element metasurface," *Electron. Lett.*, Vol. 53, 520–522, 2017.
89. Zhang, C., X. Cao, J. Gao, et al., "Shared aperture metasurface for bi-functions: Radiation and low backward scattering performance," *IEEE Access*, Vol. 7, 56547–56555, 2019.
90. Zhang, C., J. Gao, X. Cao, L. Xu, and J. Han, "Low scattering microstrip antenna array using coding artificial magnetic conductor ground," *IEEE Antennas and Wireless Propagation Letters*, Vol. 17, No. 5, 869–872, 2018.
91. Liao, W.-J., W.-Y. Zhang, Y.-C. Hou, S.-T. Chen, C. Y. Kuo, and M. Chou, "An FSS-integrated low-RCS radome design," *IEEE Antennas and Wireless Propagation Letters*, Vol. 18, No. 10, 2076–2080, 2019.
92. Jia, Y. and Y. Liu, "Low-RCS and high-gain broadband circularly polarized antenna," *2017 IEEE International Symposium on Antennas and Propagation & USNC/URSI National Radio Science Meeting*, 1923–1924, San Diego, CA, USA, 2017.
93. Dong, G., "Ultra-broadband perfect cross polarization conversion metasurface," *Opt. Commun.*, Vol. 365, No. 7, 108–112, 2015.
94. Li, Y., "An ultra-wideband linear-to-circular polarization conversion metasurface," *Chin. Phys. B*, Vol. 29, No. 10, 1–13, 2020.
95. Gao, X., X. Y. Yu, W. P. Cao, Y. N. Jiang, and X. H. Yu, "Ultra-wideband circular-polarization converter with micro-split jerusalemcross metasurfaces," *Chin. Phys. B*, Vol. 25, No. 12, 1–7, 2016.
96. Karamirad, M., C. Ghobadi, and J. Nourinia, "Metasurfaces for wideband and efficient polarization rotation," *IEEE Transactions on Antennas and Propagation*, Vol. 69, No. 3, 1799–1804, 2021.
97. Yang, X., S. Yu, N. Kou, F. Long, Z. Ding, and Z. Zhang, "Ultrathin triband reflective cross-polarization artificial electromagnetic metasurface," *Journal of Electromagnetic Waves and Applications*, Vol. 34, No. 10, 1491–1501, 2020.
98. Liu, Y., X. Dang, L. Li, and H. Yin, "Dual-wideband cross polarization conversion metasurface based on a symmetric split ring resonator," *2019 Photonics & Electromagnetics Research Symposium — Fall (PIERS — Fall)*, Xiamen, China, 2019.
99. Zheng, Q., C. Guo, and J. Ding, "Wideband metasurface-based reflective polarization converter for linear-to-linear and linear-to-circular polarization conversion," *IEEE Antennas and Wireless Propagation Letters*, Vol. 17, No. 8, 1459–1463, August 2018.
100. Yang, W., K.-W. Tam, W.-W. Choi, W. Che, and H. T. Hui, "Novel polarization rotation technique based on an artificial magnetic conductor and its application in a low-profile circular polarization antenna," *IEEE Transactions on Antennas and Propagation*, Vol. 62, No. 12, 6206–6216, 2014.
101. Yang, H., X. Liu, Y. Fan, and L. Xiong, "Dual-band textile antenna with dual circular polarizations using polarization rotation AMC for off-body communications," *IEEE Transactions on Antennas and Propagation*, Vol. 70, No. 6, 4189–4199, 2022.
102. Supreeyatitikul, N., T. Lertwiriyaprapa, and C. Phongcharoenpanich, "S-shaped metasurface-based wideband circularly polarized patch antenna for C-band applications," *IEEE Access*, Vol. 9, 23944–23955, 2021.

103. Zheng, Q., C. Guo, and J. Ding, "Wideband and low RCS circularly polarized slot antenna based on polarization conversion of metasurface for satellite communication application," *Microw. Opt. Technol. Lett.*, Vol. 60, No. 3, 679–685, 2018.
104. Liu, Y., Y.-X. Huang, Z.-W. Liu, S.-T. Cai, X.-M. Xiong, and J. Guo, "Design of a compact wideband CP metasurface antenna," *Int. J. RF Microw. Comput.-Aided Eng.*, Vol. 30, No. 10, 2020.